CONSTRUCTING AN X-RAY DIFFRACTOMETER FOR THE ANALYSIS OF THIN METAL FILMS AT HOUGHTON UNIVERSITY

By

Owen D. Fall

A thesis submitted in partial fulfillment of the
requirements for the degree of

Bachelor of Science

Houghton University

May 2025

Signature of Author……………………………………………………………………………………

Department of Physics
May 5, 2025

………

Dr. Brandon Hoffman
Professor of Physics
Research Supervisor

………

Dr. Mark Yuly
Professor of Physics

CONSTRUCTING AN X-RAY DIFFRACTOMETER FOR THE ANALYSIS OF THIN METAL FILMS AT HOUGHTON UNIVERSITY

By

Owen D. Fall

Submitted to the Department of Physics
on May 5, 2025 in partial fulfillment of the
requirement for the degree of
Bachelor of Science

Abstract

Houghton University is making an X-ray diffractometer to analyze thin metal films. X-rays are produced in a Norelco diffraction tube and detected by a Vernier Geiger tube. The angular positions of the detector and sample are controlled by stepper motors driving around a semicircular stage and are monitored by two rotary encoders each. The motors rotate at 0.68 m°/step, and there are 22.5 m°/encoder position. The sample is aligned to the axis of rotation with a linear stage. A Teensy 4.1 microcontroller controls the system via a Processing interface. Motor and encoder tests found that the angular distance between encoder positions is not uniform. An array of the number of steps between each encoder position was made for the sample and detector, which allows their angular position to be precisely known.

Thesis Supervisor: Dr. Brandon Hoffman
Title: Professor of Physics

TABLE OF CONTENTS

TABLE OF FIGURES

Chapter 1

HISTORY AND PRINCIPLES OF X-RAY DIFFRACTION

1.1. Discovery and History of X-rays

The discovery of x-rays dates back to the early 18th century, when William Crookes conducted several experiments on what he called “radiant matter”, which he believed to be a new phase of matter [1]. He employed a vacuum tube which contained a small amount of gas and a potential difference applied across two metal electrodes spaced apart in the tube. Due to the potential difference, electrons from the negative electrode traveled through the vacuum to the positive electrode, illustrated in Figure 1.

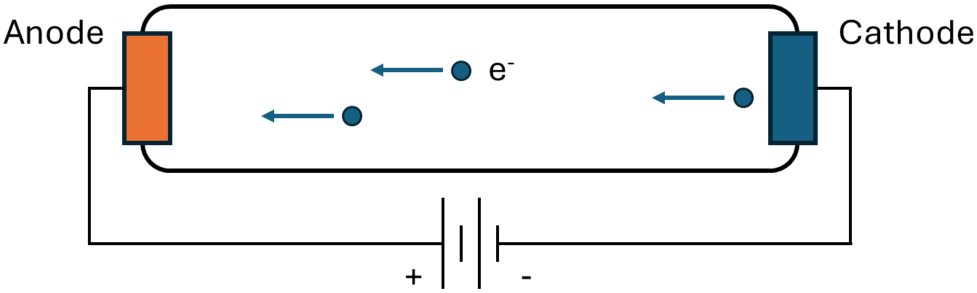

Figure 1. Crookes tube diagram. A potential difference is applied across two electrodes in a vacuum tube. Electrons from one electrode will accelerate towards the other electrode to complete the circuit.

As Crookes let in gas of different compositions, a certain phosphorescence would emit from the tube, which he called radiant matter. Unbeknownst to Crookes, this was due to the moving electrons exciting the atomic electrons of the gas, then the atomic electrons de-exciting and releasing a photon of a certain energy – phosphorescence of a certain wavelength. Crookes also noted that light emitted from radiant matter is stopped by solid matter. The energy of the electrons was not high enough to produce x-rays, but instead visible light was produced, seen by Crookes to be the phosphorescence.

X-rays, or electromagnetic waves, are produced when charged particles change their velocity. An increase in the kinetic energy of the electrons translates to a smaller wavelength of photons emitted. X-rays have a smaller wavelength than visible light and therefore have more energy. For Crookes, x-rays were produced when the electrons flew towards the positive electrode and decelerated, although he did not know this at the time.

Wilhelm Conrad Rontgen in 1896 [2] experimentally determined several characteristics of x-rays and was rewarded with their discovery. Firstly, he noticed that wood, paper, thin sheets of tin or aluminum, and fluids were transparent to x-rays [3]. This led to the well-known photo of the hand of W. C. Rontgen's wife, where a phosphorescent screen is shown illuminated in the shape of hand bones in Figure 2.

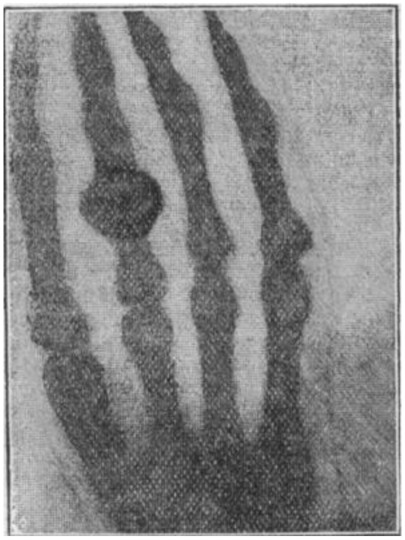

Figure 2. Photograph of x-ray plate of W. C. Rontgen's wife's hand. X-rays were shined through the flesh of the hand, but did not fully pass through the bones or the ring on the third finger. A phosphorescent screen was employed to show where the x-rays fell. Figure taken from Ref. [3].

This led Rontgen to pursue further research into x-rays. He deduced that the density of the material and its thickness is proportional to the number of x-rays absorbed. Rontgen further figured out that cathode rays (beams of electrons moving in vacuum) are the source of x-rays. While using a magnet to change the trajectory of the cathode rays, he found that x-rays originated from wherever the cathode rays struck the glass of the vacuum tube. Again, this is due to the electrons changing their velocity when striking the solid glass and producing electromagnetic waves.

X-rays have been used for a variety of scientific endeavors ever since they were formally discovered. One of the first things done with the use of x-rays was medical imaging of injuries [4]. This was a great leap forward in the medical field because then doctors were able to diagnose internal injuries more precisely without invasive surgery. X-rays were soon used for a wider range of scientific endeavors such as studying the internal structure of crystalline materials.

1.2. Crystal Analysis with X-rays

1.2.1. Characteristic and Bremsstrahlung Radiation

In order to study crystals using x-rays, the composition of this radiation must first be understood. The x-rays that emerge from an x-ray tube, like a Crookes tube, can be categorized into two different types. The first type of x-rays emitted are specific wavelengths at high intensity. These are called characteristic x-rays because the specific wavelengths depend on the material of the tube's anode. Different materials produce different x-ray wavelengths and are therefore able to be differentiated from each other. The second type of x-rays does not depend on the material. Bremsstrahlung, which is German for "breaking radiation", is a type of radiation produced from electrons altering their velocity when passing close to the atoms of the anode. As discussed before, when charged particles change their velocities, light is produced. The radiation here is x-rays because of the high initial kinetic energy of the electrons. Characteristic x-rays are especially important when studying crystals and it is important to distinguish them from the Bremsstrahlung radiation. As shown in Figure 3, the intensity of x-rays is a function of wavelength. To study crystal structures using x-rays, it is essential to know how waves interact, as light interference is the premise behind x-ray diffraction.

1.2.2. Light Interference

In 1865, James Clerk Maxwell deduced that light is comprised of electromagnetic waves [5]. Since light acts like a wave, it can interfere with itself. When two waves interact with each other, they can either build into a larger wave or collapse into a smaller wave. The larger the wave, the more intense, or bright it is. When many waves interact in this way, an interference pattern can emerge that is the sum of all the wave interactions. A diffraction grating is used to make an interference pattern of light in this way. A diffraction grating has thin slits that are cut into a screen, and when light passes through them, bright and dark bands appear projected on the surface behind. The width of the slits must be a certain order of magnitude to produce a noticeable interference pattern. This is because of the wave nature of light. When a wave passes through a gap similar in size to its wavelength, the wave spreads out on the other side, not unlike ripples in a pond, which is called diffraction. When there are many slits of the right width next to each other with waves passing through, the waves interfere with each other to produce light and dark bands, or a diffraction pattern. Measuring the distance between the diffraction pattern bands gives information about the width of the slits used in the grating.

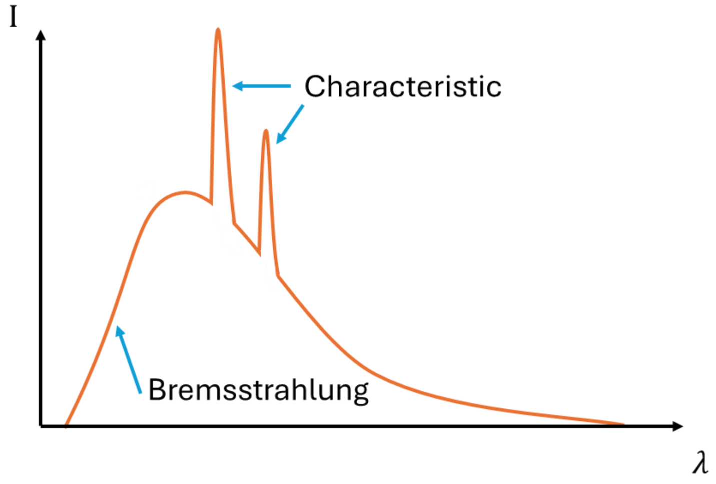

Figure 3. Characteristic and Bremsstrahlung x-rays. Intensity (I) of rays versus wavelength (λ). The broad continuous spectrum of Bremsstrahlung radiation and the precise peaks of characteristic x-rays.

A diffraction pattern can also emerge from light passing through a single thin slit, due to the principle of diffraction. Haga and Wind used this relationship to determine the approximate wavelength [6] by sending x-rays through a thin wedge-shaped slit. As the slit width decreased to the point of the wedge, the broadness of the middle band of x-rays would increase in width, represented in Figure 4. The photo plates exposed in this experiment were analyzed, and the wavelength was found to be approximately 4 x 10^{-9} m.

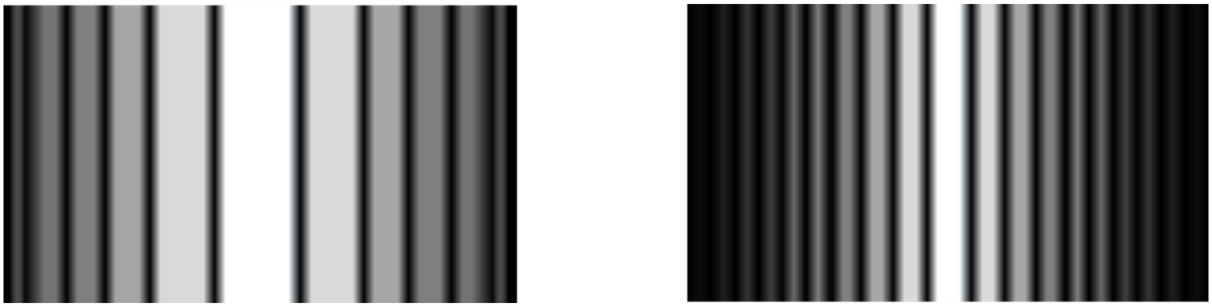

Figure 4. Single slit diffraction pattern. The right diagram shows the pattern from light diffracting through a larger slit compared to the left diagram. As the width of slit increases, the bands get closer together.

1.2.3. Max Von Laue

Since light is a wave, it can have different wavelengths. Visible light has a range of wavelengths from about 380 to 700 nm. Therefore, the slits' width in a diffraction grating must be on that same order of magnitude. Shorter wavelength light like x-rays possess wavelengths of about 1 nm, so a diffraction grating would have to have slits of similar width. In 1912, Max Von Laue proposed the idea that the analysis of crystals could be possible [7] due to the distance between atoms being of the same order of magnitude as the wavelength of x-rays. Then, crystal lattices could potentially give rise to an interference pattern not unlike a diffraction grating because the lattice spacing of crystals was similar to the measured wavelength of x-rays.

At the time, the theory of how crystals were constructed internally was established by Auguste Bravais in 1850 [8]. He formulated a set of rules that organized crystals into different groups based on their atomic structure, hexagonal and cubic, for example. These different arrangements of atoms in space were specifically called a Bravais lattice, or a space lattice. This theory was important to begin experimentally determining the internal structure of crystals. Based on the number of atoms per mole (Avogadro's number), the density of the crystal, and the assumption that crystals are regularly organized in a pattern, Laue theorized [7] that the wavelength of x-rays is similar to the plane spacing. Therefore, the wavelength of x-rays could be experimentally determined and verified. At the same time, the plane spacing of crystals could be determined, which would confirm prior theories. He worked alongside Walther Friedrich and Paul Knipping to show that crystals exposed to x-rays did in fact display an interference pattern, confirming that there was a regular pattern of atoms comprising the crystal, as seen in Figure 5.

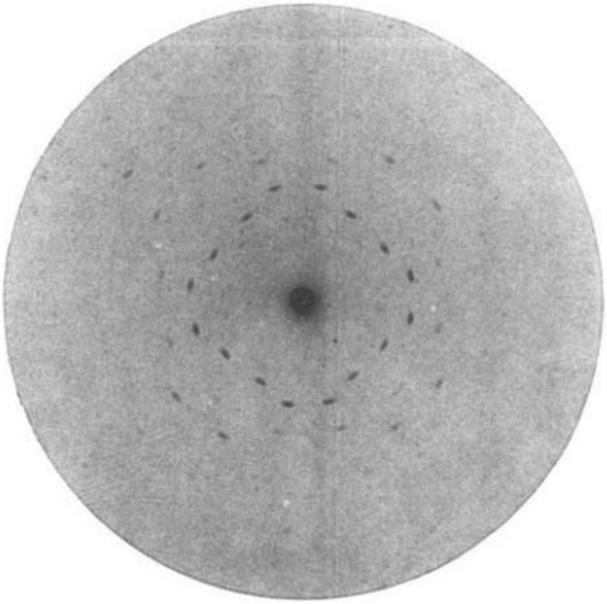

Figure 5. Laue's diffraction photograph. X-rays from a Crookes tube were aimed at a crystal of Zinc sulfide, and the reflected x-rays made an intensity spectrum on a phosphorescent screen behind the crystal. Figure taken from Ref. [9].

Laue's experiment was set up using a Crookes tube, which emitted x-rays towards the crystal in the center of several phosphorescent screens that could display the diffraction pattern at different angles [9]. X-rays from the tube spread in every direction, two sets of slits acted as collimators before the beam hit the crystal in order to have a thin stream of x-rays illuminate the sample. As crystal atoms are arranged in a repeated geometric pattern, the x-rays penetrate the crystal and reflect off of individual atoms in a certain pattern, distinctive to the crystal. The pattern depends on how the atoms are arranged internally, and Laue showed this by experimenting on different crystals and obtaining different diffraction patterns. This historical breakthrough on x-rays confirmed that they indeed carried a wave nature due to their ability to interfere with each other just as visible light.

Laue's theory of how x-rays diffracted through crystals was mathematically challenging because he calculated the diffraction due to scattering from each individual atom [7], producing a diffraction pattern when summing all of the interactions together. William

Henry Bragg and his son William Lawrence Bragg simplified the mathematics by modeling the scattering of x-rays off of crystal planes made by the conglomeration of atoms in the crystal. Using this method, the Braggs were eventually able to mathematically interpret the photographs that Laue obtained.

1.2.4. Miller Indices

In 1839, William Hallowes Miller described a geometric way of thinking about crystal planes [10], which was used to mathematically differentiate diffraction patterns, and is now the common convention when speaking on the subject. Every crystal structure has a repeated pattern of atoms that can be represented with three vectors,

$$\vec{R} = \mathrm{A}\overrightarrow{a_1} + \mathrm{B}\overrightarrow{a_2} + \mathrm{C}\overrightarrow{a_3}, \tag{1}$$

where A, B and C are integers. Vectors $\overrightarrow{a_1}$, $\overrightarrow{a_2}$, and $\overrightarrow{a_3}$ are not necessarily orthogonal to each other and the lengths are the smallest distance in their direction that maintains translational symmetry. These vectors point in three different directions and describe a 3D crystal shape. An ideal crystal, i.e. a cube, parallelepiped, etc., has translational symmetry for all $\vec{R}$. For the simple cubic shape in Figure 6, the vectors $\overrightarrow{a_1}$, $\overrightarrow{a_2}$, and $\overrightarrow{a_3}$ point along the x, y, and z axis, respectively.

When analyzing x-ray diffraction from crystal planes, it is convenient to define another vector which points perpendicular to the planes and has the same units of inverse distance as an x-ray wave vector. The vector,

$$\overrightarrow{G_{\mathrm{hkl}}} = \mathrm{h}\overrightarrow{b_1} + \mathrm{k}\overrightarrow{b_2} + \mathrm{l}\overrightarrow{b_3}, \tag{2}$$

describes the normal direction to the crystal plane, where h, k, l are integers and $\left|\overrightarrow{b_\mathrm{j}}\right| = \frac{2\pi}{|\overrightarrow{a_j}|}$, with $\overrightarrow{b_j}$ being normal to the plane formed by the other two real space vectors. This can be visualized in Figure 6, where a plane intersects a set of axes that happen to be orthogonal to each other, which are labeled x, y, and z.

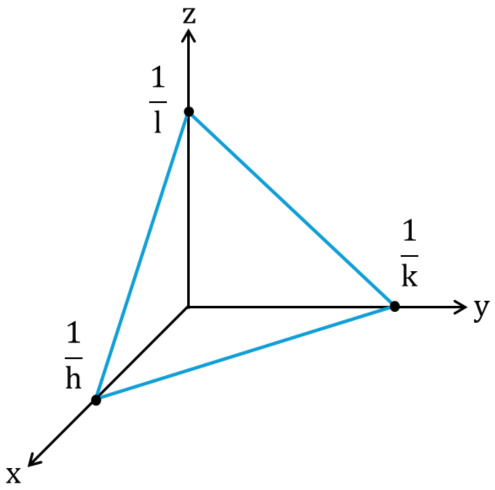

Figure 6. Diagram demonstrating Miller Indices. A crystal plane made by three atoms intersects points 1/h, 1/k, and 1/l as shown. The Miller Indices (hkl) represent the reciprocal distances of intersection with the plane and the x, y, and z axes.

The Miller Indices (hkl) describe the orientation of crystal planes. The vector $\vec{G}_{\text{hkl}}$ points normal to the plane in Figure 6. This allows different orientations of planes to be mathematically grouped. These Miller Indices are what Bragg used to group different crystal diffraction patterns [10] with the same experimental setup used by Laue described earlier. Bragg used the position of the diffraction spots to figure out corresponding (hkl) values.

Bragg noted that in the Laue photographs, the spots of x-rays correspond to a certain arrangement of atoms in the crystal. In Bravais lattices, atoms act as points in space and are arranged in different patterns that repeat in the whole crystal. In fact, Bragg says that the atoms can always be thought of as the corners of many parallelepipeds. A parallelepiped is a three-dimensional shape with six faces of parallelograms. If a pulse of light rays interacts with this space lattice, pulses would be diffracted from planes made from atoms. Because of the specific lattice arrangement, the pulses would combine in certain directions more than others, creating a certain pattern of diffracted x-rays as seen by Laue in Figure 5.

1.2.5. Bragg's Law

William Lawrence Bragg wanted to simplify the theory that x-rays diffract off of individual atoms in the lattice. The use of Miller Indices shows that the diffraction pattern of crystals can be thought of as being due to crystal planes. Incident x-rays reflect off the many planes inside the crystal, combining at certain spots on the photo plate. The reason that some spots are more intense than others is because some angles are more probable to reflect more x-rays than others. Bragg produced a straightforward way of mathematically describing how x-rays reflect off crystal planes. This paved the way for the creation of a machine that helped find the internal structure of many crystals.

1.3. Early X-ray Spectrometers

1.3.1. Bragg Spectrometer

William Henry Bragg and William Lawrence Bragg constructed an x-ray spectrometer [11] in order to show the principle of their famous theory. In their joint work where they originally came up with the theory, the machine they built used a Crookes type tube for the source of x-rays. Similar to Laue's experimental setup, the x-rays were sent through two sets of slits that acted as collimators before the beam hit the crystal. This was to make the beam as aligned as possible to the crystal for maximum accuracy. Unlike Laue's original setup, this one featured a rotating detector arm and a rotating sample holder through the same axis, photographed in Figure 7.

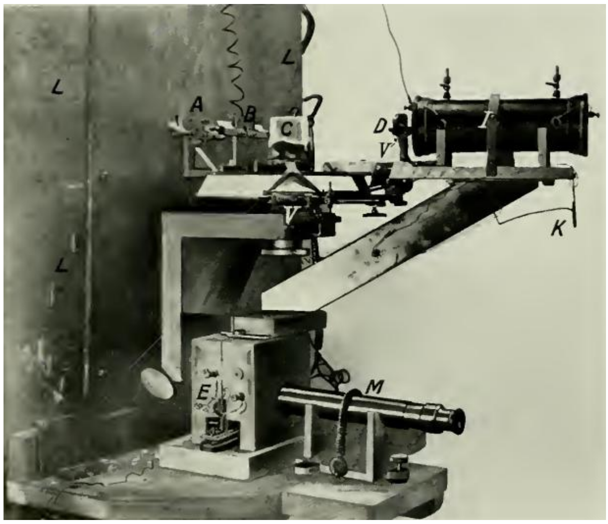

Figure 7. Bragg spectrometer. X-rays were produced by a tube behind a lead shield L, collimated through slits A and B towards the crystal C. An ionization chamber D was the detector, which relayed the information through wire K to electroscope E [11]. The reading was precisely read through microscope M. V and V' are the verniers on the rotating elements of the setup.

As x-rays intersected the sample, reflected x-rays would scatter in every direction, some directions more than others. Before any rays made it to the detector, they would again be subjected to a thin slit that made the measurements more precise. The detector was an ionization chamber, which was filled with a gas that ionized when x-rays passed through. The ionized gas produces a current which is proportional to the intensity of x-rays. This current was read using a Wilson Tilted Electroscope [11], which uses the repelling force of like charges to push a gold leaf around a voltage scale. The two Braggs used a microscope to read the amount of current from the ionization chamber, which told them proportionally how many x-rays reflected at certain angles. A grounding wire was used to remove built up charge on the gold leaf, so that more measurements could be made for new angles. As the detector and crystal rotated, x-rays would reflect off of different planes at different intensities. This, coupled with Bragg's law, would describe the internal arrangement of atoms in the crystal lattice. Tangent screws were used in the contraption to have a precise and controlled rotation of sample and detector. A common technique used was to rotate the crystal sample at half the rate of the detector. This was to maintain the Bragg condition of an angle Θ made with the incident x-ray beam and the sample face, and an angle 2Θ made with the incident x-ray beam and the reflected x-rays. The importance of this was to keep the angles of incidence and reflection constant throughout data collection. This technique was useful to look for planes oriented parallel to the sample surface.

1.3.2. X-ray Spectra Analysis

Bragg did many experiments on the spectra produced from the diffraction of x-rays through different crystals. The spectra produced were from carefully measuring the ionization current from the detector and plotting the values against the angle between the detector and incident x-ray beam, as seen in Figure 8.

Spectra of the two materials, KCl and NaCl, with the planes (100), (110), and (111) facing the incoming x-rays, are separately graphed. To analyze the data, he assumed that the KCl crystal is in the cubic category of Bravais lattice types, since those crystals often are cubic in appearance. From there, the ratios of the distances between planes can be obtained for each orientation, which should be equal to a set ratio for each Bravais lattice type. In Figure 9, a face centered cubic (FCC) lattice is shown, which can represent a KCl crystal, other ionic compounds, and even some elements.

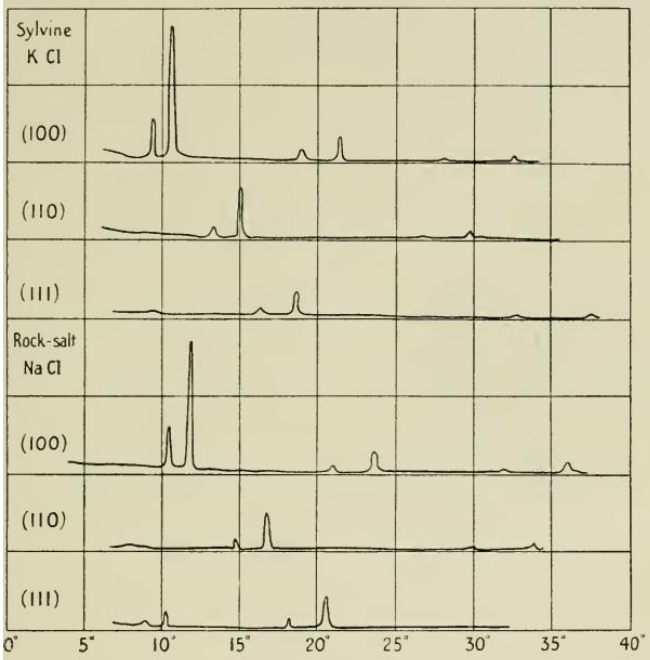

Figure 8. Intensity of x-rays vs. scattering angle. KCl and NaCl crystals are shown, each separately cut so that the x-rays were incidence to the faces (100), (110), and (111). Figure from Ref. [11].

This cube pattern is repeated throughout the whole crystal, so the planes repeat in a parallel manner. The distance between repeated (100) planes is set to 1, so that the distance between (110) planes become $1/\sqrt{2}$ and $1/\sqrt{3}$ for (111). These values are each associated with the inverse distances from one plane to the next plane, Miller Indices h, k and l. The distance between planes is related to the incident angle and can be determined using XRD. Each crystal type has a different dominant plane spacing, and the same approach can be extrapolated for more intricate crystal structures, where the planer distances and the shape of the lattice are slightly different. The crystal NaCl was theorized to be FCC from external observation and the plane spacing d calculated knowing its composition. This led Bragg to use XRD to make more a precise measurement of the wavelength of x-rays than that of Haga and Wind [6].

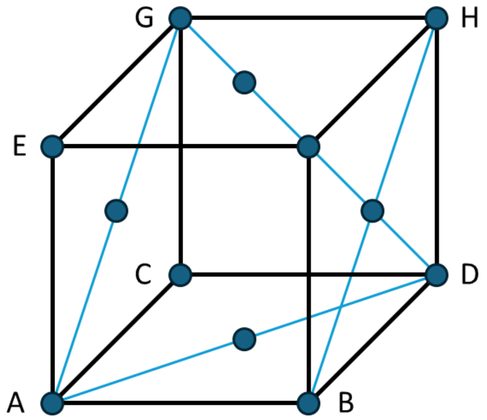

Figure 9. Face centered cubic structure. A cubic crystal made with eight atoms in each corner, and six face centered atoms. Three plane orientations, (100), (110), and (111) are given by vertices AEGC, ABHG, and ADG, respectively.

1.4. Thin Metal Films

The history of using x-rays to study crystals has evolved since the early 1900s. In modern times, we have electronics that rely on many different components, some of which are made using thin metal films. They are an essential part of modern technology, and also the topic of much research. The adjective "thin" refers to the fact that these films are much smaller in one dimension than the other two dimensions. Usually, thin films are nanometers thick in size. They are produced using a variety of methods; however, a common method is called physical vapor deposition. The metal of choice sits in a cup or crucible that is heated by a hot filament through thermionic emission of electrons, or directly through the passage of current. In a vacuum, the metal will evaporate at a lower temperature than if it were at atmospheric pressure because the vapor pressure is greater than the chamber pressure. When the metal reaches this point, metallic gas fills the vacuum chamber. A substrate, commonly made of silicon glass, is placed inside the chamber so that some of the metal is deposited to its surface, forming layers. Eventually this makes a metal film nanometers thick. The arrangement of atoms in the film are crystal structures. This gives rise to the interesting research surrounding thin metal films and x-ray diffraction. If x-rays could be used to determine the atomic arrangement of crystal chunks, then maybe they could also be used to analyze thin metal films.

1.4.1. Characteristics of Thin Films

There are several different characteristics of thin metal films that are important to consider. When producing films, metal atoms are deposited on a substrate, and they arrange themselves in a particular way. At first, the map of atoms is random, but as more are deposited, groups of atoms start to form. These are called grains and as the film is being built, these grains grow and form boundaries between each other. The size and number of grains depends on the deposition parameters like deposition temperature, rate, and time. Higher temperature atoms are able to move around and cluster easier on the substrate, meaning fewer and larger grains will form. These grains grow until their boundaries reach each other, creating a completed film. Then more layers of atoms can form on top to make the film thicker. A grain's orientation is defined by the plane that is parallel to the sample surface. For example, a grain composed of (111) orientated planes would form by layering (111) planes parallel to the substrate surface. Investigations on the structure of thin metal films were carried out throughout the 1900s, advancing the field of both thin metal films and x-ray diffraction.

In 1935, W. A. Wood observed differences in thin nickel and chromium thin films through the use of x-ray diffraction [12]. The properties of metal that have been deposited on a substrate were different than that of normal metal, such as hardness and lattice distortion. Broad intensity peaks from x-ray diffraction indicated a hard material, while softer materials produced more precise peaks. Wood's results were consistent with the theory developed by Sherrer [13], which found the grain size inversely proportional to the width of diffracted x-ray intensity peaks. Finally, the orientations of the crystal planes depended heavily on the deposition conditions like temperature of the evaporated metal. All of these characteristics affect the electrical and mechanical properties of the films, which is important for understanding how to make electronics more efficient. However, many unanswered questions emerge about these characteristics when considering what thin metal films are used for. When they undergo mechanical stress or severe temperatures post-production, the impact to the hardness and the lattice structure is unknown. Also, the fundamental question of why the crystals form certain grain orientations over others is yet to be answered. These are important considerations for producing quality films.

1.4.2. Leading Research in Thin Films

Through working with improved XRD systems, researchers have found that crystals prefer some orientations to others due to differences in energy. For example, as-deposited silver films are mostly (111) orientation because this orientation has densely packed atoms which are closer together. This is the lowest surface energy state of the atoms, and therefore the preferred arrangement. Through a process called annealing, thin films are heated to several hundred Kelvins for an extended period of time, sometimes many hours. This allows the grains to restructure and form different textures. Films of face centered cubic material, like copper and silver, transform from predominantly (111) to (100) texture [14]. X-ray diffraction techniques are commonly used to find the textures of films. ZnO films were investigated and found to have a preferred orientation of (002) [15]. The deposition parameters were also found to be of great influence on the texture composition. One theory of the driving force mitigating this transformation deals with the energies required to hold the film together and on the substrate. During annealing, the added thermal energy could promote atoms to reorganize and transform to lower energy state grains. However, this theory has been called into question because of experiments that hint at a piece missing from the theory [16]. Recent investigations have revealed that film thickness could be the dominating factor behind texture transformations [17]; however, the reason behind this dependency is unknown, and it is likely not the only factor responsible. This search for the driving forces behind texture transformation is motivated by the need for better films. The boundaries between grains, the size of grains, film textures and stresses all impact the films mechanical and electrical properties. X-ray diffractometry is an essential tool needed to analyze the structures of thin metal films.

Possessing the knowledge to produce specifically tailored films for electrical components is an important part of manufacturing thin films. To do this, Houghton University and Cornell University have conducted research into the driving forces behind texture transformation using an x-ray diffractometer. A publication [18, 19] by several authors including Cornell professor Shefford P. Baker reported that texture transformations were most likely due to many driving forces, one of which was the density of twin boundaries in film grains. Twin boundaries, or stacking faults, are mirrored layers amidst deposited layers on a film. There is an orderly arrangement that the layers of atoms follow, but sometimes there is a twin boundary which disrupts this pattern. These faults are in a higher energy state than otherwise and therefore could contribute to texture transformations. More research is needed to fully determine a theory that explains the driving forces at a deeper level.

1.5. Houghton University's X-ray Diffractometer

At Houghton University, there is an x-ray diffractometer (XRD) under production, made to conduct thin film research. The Houghton XRD is modeled after similar geometry to Bragg's original spectrometer, so as to analyze the planes in a crystal sample. The goal with this project is to be able to conduct research on thin metal films that are produced in Houghton University's physical vapor deposition chamber. The XRD is able to have the classic ϴ-2ϴ geometry used by Bragg originally and can be used for other scan methods such as rocking curve scans, which holds the detector steady at a crystal plane angle and rotates the sample over small angles. Two aluminum arms powered by stepper motors revolve about an axle which holds the arms together. X-rays created via a Norelco x-ray tube [20] are incident upon the sample which can be rotated by one of the arms and is situated directly above the axle. The second arm can rotate independently of the other and has a detector mounted to it. The detector is a Geiger tube which is capable of detecting radiation and converting it to electrical current. The x-rays are collimated through thin slits in the x-ray tube itself, but also through the use of a thick steel pipe that points towards the sample. The angles of the detector and sample arm are monitored by four rotary encoders which are connected to the axle, two encoders for each arm. The motors and encoders send and receive data through a Teensy 4.1 microcontroller which is controlled by a computer program via Arduino code. The x-ray tube anode is held at 40 kV relative to the filament, or the cathode. A battery and buck converter circuit supply current through the filament. Due to the high potential across the anode and cathode inside the tube, electrons accelerate towards the Cu anode and produce characteristic Cu x-rays and Bremsstrahlung x-rays. For safety reasons, the whole machine is surrounded by a steel box. Along the path of incident x-rays, lead bricks are stacked so as to minimize the radiation leaving the box. Several switches are used on the outside of the box to ensure that if it is opened, the power is shut off and everything is safely grounded. A

Geiger counter is used to verify that the radiation levels surrounding the box are at background level.

Chapter 2

ELECTROMAGNETIC RADIATION

2.1. Electromagnetic Waves

2.1.1. Maxwell's Equations

In the mid-nineteenth century, James Clerk Maxwell made improvements to the established equations of electrodynamics of that period, which famously became known as Maxwell's equations. The divergence of an electric field, $\vec{E}$, is

$$\vec{\nabla} \cdot \vec{E} = \frac{1}{\epsilon_0} \rho \tag{3}$$

where ϵ_0 is the permittivity of free space and ρ is the charge per unit volume. The expression is equal to zero because electromagnetic waves are assumed to travel through free space, where ρ is zero. Similarly, the divergence of a magnetic field, $\vec{B}$, is

$$\vec{\nabla} \cdot \vec{B} = 0. \tag{4}$$

Because there are no magnetic monopoles, the field lines form closed loops. The third and fourth equations describe the curl of an electric and magnetic field, respectively. The curl of an electric field,

$$\vec{\nabla} \times \vec{E} = -\frac{\partial \vec{B}}{\partial t}, \tag{5}$$

is related to the time derivative of the magnetic field. This relationship was deduced through experiments that showed a changing magnetic field induces an electric field. The next and final of Maxwell's equations gives a similar symmetrical relationship to the previous one, where the curl of a magnetic field is

$$\vec{\nabla} \times \vec{B} = \mu_0 \vec{J} + \mu_0 \epsilon_0 \frac{\partial \vec{E}}{\partial t}, \tag{6}$$

where μ_0 is the permeability of free space and $\vec{J}$ is the volume current density. The volume current density is zero because the charge density ρ is zero.

Equations (5) and (6) couple the electric and magnetic fields. To decouple these quantities, the curl can be applied to both equations. When taking the curl of Equation (5), a vector identity,

$$\vec{\nabla} \times \left(\vec{\nabla} \times \vec{A}\right) = \vec{\nabla}\left(\vec{\nabla} \cdot \vec{A}\right) - \nabla^2 \vec{A}, \tag{7}$$

can be used in order to obtain

$$\vec{\nabla} \times \left(\vec{\nabla} \times \vec{E}\right) = \vec{\nabla}\left(\vec{\nabla} \cdot \vec{E}\right) - \nabla^2 \vec{E} = \vec{\nabla} \times \left(-\frac{\partial \vec{B}}{\partial t}\right). \tag{8}$$

From here, each side of the expression can be addressed separately:

$$\vec{\nabla} \times \left(\vec{\nabla} \times \vec{E}\right) = \vec{\nabla}\left(\vec{\nabla} \cdot \vec{E}\right) - \nabla^2 \vec{E} = -\nabla^2 \vec{E} \tag{9}$$

$$\vec{\nabla} \times \left(-\frac{\partial \vec{B}}{\partial t}\right) = -\frac{\partial}{\partial t}\left(\vec{\nabla} \times \vec{B}\right) = -\mu_0 \epsilon_0 \frac{\partial \vec{E}}{\partial t} \tag{10}$$

using the fact that the divergence of the electric field is zero and the curl of the magnetic field is in Equation (6).

Next, taking the curl of Equation (6) gives

$$\vec{\nabla} \times \left(\vec{\nabla} \times \vec{B}\right) = \vec{\nabla}\left(\vec{\nabla} \cdot \vec{B}\right) - \nabla^2 \vec{B} = \vec{\nabla} \times \left(\mu_0 \epsilon_0 \frac{\partial \vec{E}}{\partial t}\right) \tag{11}$$

and in the same way as before, the expression becomes

$$\mu_0 \epsilon_0 \frac{\partial}{\partial t}\left(\vec{\nabla} \times \vec{E}\right) = -\mu_0 \epsilon_0 \frac{\partial^2 \vec{B}}{\partial t^2}. \tag{12}$$

Equation (7) can be used, with $\vec{\nabla} \cdot \vec{E}$ and $\vec{\nabla} \cdot \vec{B}$ both zero, to obtain

$$\nabla^2 \vec{E} = \mu_0 \epsilon_0 \frac{\partial^2 \vec{E}}{\partial t^2}, \qquad \nabla^2 \vec{B} = \mu_0 \epsilon_0 \frac{\partial^2 \vec{B}}{\partial t^2}. \tag{13}$$

This is the solution to the 3-D wave equation, giving decoupled second-order differential equations for electric and magnetic fields. These differential equations can be solved using a change of variables. For XRD, only one-dimensional waves need to be considered because of the one-dimensionality of successive crystal planes.

2.1.2. The D'Alembert Solution to the One-Dimensional Wave Equation

Let's say we have an arbitrary function, $u(x,t)$, with distance x and time t as independent variables. This function solves

$$\frac{\partial^2 u}{\partial x^2} = \frac{1}{s^2}\frac{\partial^2 u}{\partial t^2}, \tag{14}$$

where the second partial derivatives with respect to distance and time will have to be found. The constant $\frac{1}{s^2}$ becomes important later. The coordinate system of the function can be changed by defining two new independent variables:

$$a = x + vt \tag{15}$$

$$b = x - vt, \tag{16}$$

where v is a velocity. Now, the second partial derivatives with respect to distance and time will have to be found with respect to a and b also. Starting with the distance derivative, the use of the chain rule results in

$$\frac{\partial u}{\partial x} = \frac{\partial u}{\partial a}\frac{\partial a}{\partial x} + \frac{\partial u}{\partial b}\frac{\partial b}{\partial x}. \tag{17}$$

The second derivative of the function with respect to x is

$$\frac{\partial^2 u}{\partial x^2} = \frac{\partial}{\partial x}\left[\frac{\partial u}{\partial x}\right] = \frac{\partial}{\partial x}\left[\frac{\partial u}{\partial a}\frac{\partial a}{\partial x} + \frac{\partial u}{\partial b}\frac{\partial b}{\partial x}\right] \tag{18}$$

and by the product rule

$$\frac{\partial^2 u}{\partial x^2} = \frac{\partial}{\partial x}\left[\frac{\partial u}{\partial a}\right]\frac{\partial a}{\partial x} + \frac{\partial u}{\partial a}\frac{\partial}{\partial x}\left[\frac{\partial a}{\partial x}\right] + \frac{\partial}{\partial x}\left[\frac{\partial u}{\partial b}\right]\frac{\partial b}{\partial x} + \frac{\partial u}{\partial b}\frac{\partial}{\partial x}\left[\frac{\partial b}{\partial x}\right]. \tag{19}$$

In this expression, the first and third terms can be simplified using the chain rule and the expression results to

$$\frac{\partial^2 u}{\partial x^2} = \frac{\partial}{\partial a}\frac{\partial u}{\partial a} + \frac{\partial}{\partial b}\frac{\partial u}{\partial a} + \frac{\partial u}{\partial a} + \frac{\partial}{\partial b}\frac{\partial u}{\partial b} + \frac{\partial}{\partial a}\frac{\partial u}{\partial b} + \frac{\partial u}{\partial b} \tag{20}$$

using the fact that the derivative of a and b with respect to x is 1.

The same process can be taken with the derivative of the function with respect to time. In this case, the expression can be simplified to

$$\frac{\partial^2 u}{\partial t^2} = \frac{\partial}{\partial a}\frac{\partial u}{\partial a}v^2 - \frac{\partial}{\partial b}\frac{\partial u}{\partial a}v^2 + \frac{\partial u}{\partial a}v^2 + \frac{\partial}{\partial b}\frac{\partial u}{\partial b}v^2 - \frac{\partial}{\partial a}\frac{\partial u}{\partial b}v^2 + \frac{\partial u}{\partial b}v^2 \tag{21}$$

due to Equation (15) where $\frac{\partial a}{\partial t} = v$ and $\frac{\partial b}{\partial t} = -v$.

Finally, substitute these new second derivatives into Equation (14), which yields a simplified expression of

$$\frac{\partial}{\partial b}\frac{\partial u}{\partial a} + \frac{\partial}{\partial a}\frac{\partial u}{\partial b} = -\frac{\partial}{\partial b}\frac{\partial u}{\partial a} - \frac{\partial}{\partial a}\frac{\partial u}{\partial b} \tag{22}$$

when $v = s$. Since the order that the derivatives are taken does not matter, this expression can be written as

$$\frac{\partial^2 u}{\partial a \partial b} = 0, \tag{23}$$

a second order linear differential equation. The solution can be found by first taking the integral of both sides with respect to a and then b. In this case the expression becomes

$$\int \frac{\partial^2 u}{\partial a \partial b}\, da = \frac{\partial u}{\partial b} + c_1(b) = \int 0 \, da = c_2(b) \tag{24}$$

and therefore

$$\frac{\partial u}{\partial b} = h(b), \tag{25}$$

where $h(b) = c_2(b) - c_1(b)$.

Similarly, integrating both sides with respect to b is

$$\int \frac{\partial u}{\partial b}\, db = u(a,b) + c_3(a) = \int h(b)\, db = g(b) + c_4(a) \tag{26}$$

giving the solution to the wave equation for an arbitrary function as

$$u(a,b) = f(a) + g(b) \tag{27}$$

where $f(a) = c_4(a) - c_3(a)$ and $g(b)$ is the result of integrating $h(b)$. The function can be written in terms of the original variables, distance and time, as

$$u(x,t) = f(x+vt) + g(x-vt). \tag{28}$$

Setting f or g to zero will result in a right moving wave or a left moving wave respectively. This function depends on $x \pm vt$, moving through distance and time with a maintained form. For this application, only the 1-D case of the electromagnetic wave from Equation (13) is being considered. Therefore, the solution to the electric and magnetic field equations are also of the same form as Equation (28). Their solutions are then in the form

$$u(x,t) = g(x-vt) \tag{29}$$

because in this case, x-rays are issuing from the source and moving to the right (i.e. $f = 0$).

This solution can be written as an integral of sine waves through a Fourier transform. The solution then becomes

$$\vec{E}(z,t) = \int_0^{\infty} \left[\vec{E}_{01}(k)\sin\big(k(z-vt)\big) + \vec{E}_{02}(k)\cos(k(z-vt))\right] dk, \tag{30}$$

with $k = \frac{2\pi}{\lambda}$, where λ is the wavelength and $k_{max} = \lambda_{min}$. The electric field then becomes

$$\vec{E}(z,t) = \int_0^{\lambda_{min}} \left[\vec{E}_{01}(k)\sin(kz-\omega t) + \vec{E}_{02}(k)\cos(kz-\omega t)\right] dk, \tag{31}$$

and the magnetic field similarly is

$$\vec{B}(z,t) = \int_0^{\lambda_{min}} \left[\vec{B}_{01}(k)\sin(kz-\omega t) + \vec{B}_{02}(k)\cos(kz-\omega t)\right] dk, \tag{32}$$

where $\omega = kv$. These fields are waves traveling in the z-direction.

These electromagnetic waves come from the source and are composed of multiple wavelengths due to Bremsstrahlung and characteristic radiation, seen in Figure 3. Bremsstrahlung is a continuous spectrum of energy essentially acting as background. Characteristic radiation is unique energy peaks that are very intense compared to Bremsstrahlung. Therefore, the characteristic radiation peaks can be distinguished from the

Bremsstrahlung radiation due to the difference in intensity at certain wavelengths. Max Planck stated

$$E = hf = \frac{hc}{\lambda}, \tag{33}$$

relating the frequency of radiation to energy. Therefore, for the purposes of this setup, the electric field can be written as

$$\vec{E}(z,t) = \vec{E}_0 \cos(kz - \omega t + \delta_E) \tag{34}$$

with δ_E as a phase shift. The coordinates have been defined such that $\vec{E}(z,t)$ is maximized at (0,0), which causes $E_{01} = 0$. The magnetic field can similarly be written as

$$\vec{B}(z,t) = \vec{B}_0 \cos(kz - \omega t + \delta_B) \tag{35}$$

where the amplitude must be defined in terms of the electric field amplitude. To relate these two phase shifts, consider Equation (5) where

$$\vec{\nabla} \times \vec{E} = \frac{\partial}{\partial z}\hat{k} \times \vec{E}_0 \cos(kz - \omega t + \delta_E) = -k\vec{E}_0 \sin(kz - \omega t + \delta_E) \tag{36}$$

and

$$-\frac{\partial \vec{B}}{\partial t} = \frac{\partial}{\partial z}\vec{B}_0 \cos(kz - \omega t + \delta_B) = -\omega\vec{B}_0 \sin(kz - \omega t + \delta_B) \tag{37}$$

so that

$$k\vec{E}_0 = \omega\vec{B}_0, \tag{38}$$

implying that the phase shifts δ_E and δ_B are equal. The amplitude of the magnetic field then becomes

$$B_0 = \frac{k}{\omega}E_0 = \frac{1}{v}E_0. \tag{39}$$

The solutions to the electric magnetic field imply that their velocity v can be found using the fact that the solutions to the wave equation are functions of $x \pm vt$. Solving the electromagnetic field equation in this way yields that the constant in (14) corresponds to

$$s^2 = \frac{1}{\mu_0 \epsilon_0} \tag{40}$$

and solving for s gives

$$s = \frac{1}{\sqrt{\mu_0 \epsilon_0}} = \frac{1}{\sqrt{(4\pi \times 10^{-7}\mathrm{H/m}) \times (8.85 \times 10^{-12}\mathrm{F/m}\,)}} = 3.00 \times 10^8 \frac{m}{s}, \tag{41}$$

the speed of light. Therefore, electromagnetic radiation is light and can interfere like any wave.

2.2. Light Interference

The electric field in a region can be written as a vector sum of electric fields from all sources, resulting in Equation (34). The same can be said about magnetic fields with Equation (35). This principle is called superposition. When there is a superposition of plane waves, i.e. electric or magnetic, the amplitude of the resultant wave depends on the phase shift of the summed waves.

Here, two electric fields are added together,

$$\overrightarrow{E_T}(z,t) = \overrightarrow{E_0}\cos(kz - \omega t + \delta_1) + \overrightarrow{E_0}\cos(kz - \omega t + \delta_2), \tag{42}$$

the only difference being their phase shifts. Using the superposition of trigonometric functions identity,

$$\cos(\alpha) + \cos(\beta) = 2\cos\left(\frac{\alpha + \beta}{2}\right)\cos\left(\frac{\alpha - \beta}{2}\right), \tag{43}$$

the electric fields becomes

$$\overrightarrow{E_T}(z,t) = 2\overrightarrow{E_0}\cos\left(kz - \omega t + \frac{\delta_1 + \delta_2}{2}\right)\cos\left(\frac{\delta_1 - \delta_2}{2}\right) \tag{44}$$

where now we have a total electric field, $\overrightarrow{E_T}$, that is one sinusoidal function that depends on the phase shift , $\delta = \frac{\delta_1 + \delta_2}{2}$ between the two, with a new amplitude of $2E_0 \cos\left(\frac{\delta_1 - \delta_2}{2}\right)$ at the detector.

For example, if two sine waves of the same frequency are out of phase by 180°, the resultant wave amplitude is zero. But anywhere between 0 and 180°, the waves do not cancel out fully.

In this case, the electromagnetic waves have the same frequency but can also be out of phase. Therefore, the path length difference, L, between electromagnetic waves is important when considering the intensity of rays from a source. The phase shift between two waves of the form of Equation (34) is

$$\delta = Lk, \tag{45}$$

where L between two waves is the difference in distance that the two traveled. If $L = \mathrm{n}\lambda$, then the phase shift is $\delta = \mathrm{n}2\pi$.

2.2.1. Bragg's Law

Now consider electromagnetic waves moving towards a crystal lattice at an angle. As discussed in Section 1.2.4, crystals are composed of a repeated pattern of atoms that can be thought of as forming planes in the crystal. Different films will have different sets of orientations that are most prevalent in them. For example, Ag deposited films are predominantly (111) orientation. To study the orientations, and therefore atomic arrangements of atoms, the properties of light are used. In this specific case, x-rays are used because their wavelength is on the order of magnitude of the atomic spacing of crystals. This means that diffraction patterns will likely emerge from incident x-rays on a crystal lattice. A diffraction pattern is made when waves interfere with each other and produce intense and dark points where there is constructive and destructive interfere. Crystals usually produce a diffraction pattern with some of these intense spots from the x-rays that are nearly perfectly constructive with each other. The lattice can be modeled as an infinite set of continuous parallel planes. The waves will reflect off of the planes, each wave experiencing a new path length difference (PLD) because the planes are deeper into the crystal. The PLD is then related to the angle of incidence, as seen in Figure 10.

The first wave reflects off of the top plane while the second wave reflects off of the second plane, and so on. The second wave travels a larger distance than the first wave due to the position of the second plane. This PLD is $2d \sin\theta$. Sir William Henry Bragg noticed [11] that if the PLD is equal to an integer number, n, of the wavelength, λ,

$$\mathrm{n}\lambda = 2d \sin\theta, \tag{46}$$

the interference will be at a maximum coherence, producing the highest intensity.

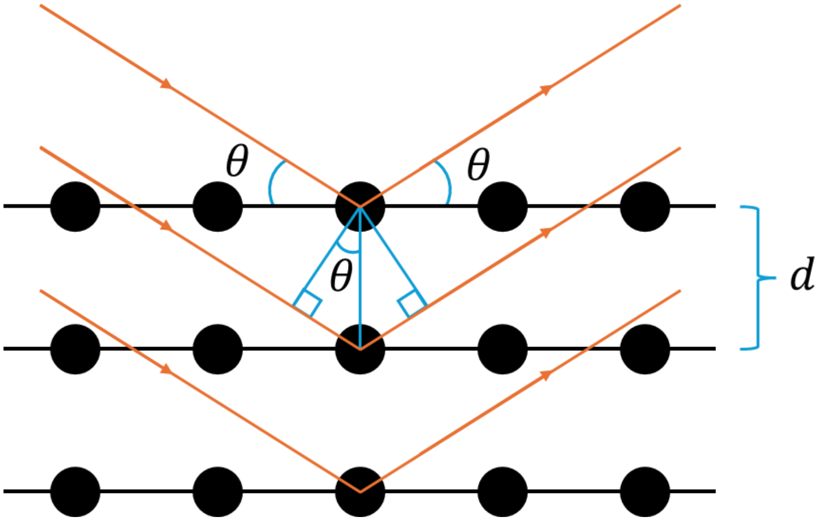

Figure 10. Bragg's Law Diagram. Rays represented by arrows are incident to a crystal lattice of spacing d. The angles of incidence and reflection are both θ. The blue triangles show the geometry for the PLD.

When radiation interacts with a crystal, there is a certain intensity of incident radiation that is due to the amplitude of the electromagnetic waves. This amplitude depends on the phase shift between waves and is $2E_1 \cos\left(\frac{\delta_1-\delta_2}{2}\right)$ from Equation (44). The Poynting vector,

$$\vec{S} = \frac{1}{\mu_0}(\vec{E} \times \vec{B}), \tag{47}$$

describes the power flux of electromagnetic radiation in the direction of propagation. Some x-rays will reflect off of the crystal planes and interfere with each other to create varying intensity at the detector. The amount of radiation associated with each angle can be described with the Poynting vector, as it describes the amount of radiation passing through an area per time. In this way, an intensity plot of a diffraction pattern can be analyzed to find the amount of radiation hitting a detector per second. This will show at what angles give maximum coherence of x-rays, and thus revealing which crystal planes are present.

2.3. X-Ray Production

X-rays are produced in a vacuum tube, like a Crookes tube, where there is a high potential between the anode and cathode which are separated in the tube. Due to the high potential difference, electrons are able to traverse through the vacuum and strike the anode. When some fast electrons come close to the atoms of the anode material, they are deflected by the positive nuclei or the negative electron clouds. When a charged particle alters its velocity, there is radiation emitted, pictured in Figure 11 . According to the Larmor formula,

$$P = \frac{\mu_0 q^2 a^2}{6\pi c}, \tag{48}$$

the power emitted P is proportional to a^2, where a is the acceleration of the charged particle. In the case of an electron, the charge q is 1 e so there is power emitted when it changes its velocity. This acceleration releases energy in the form of an electromagnetic wave.

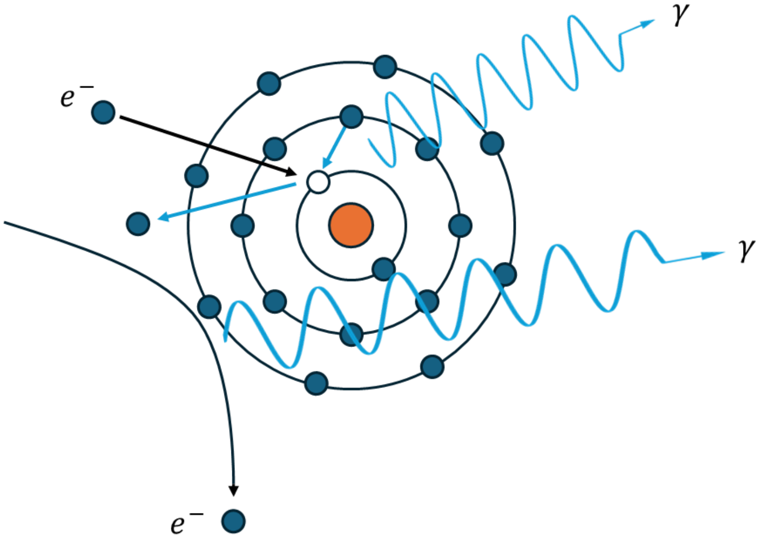

Figure 11. Bremsstrahlung and characteristic radiation. An electron (blue) passes close to an atom and alters its speed due to the positive charge of the nucleus (orange). This change in momentum of the electron releases energy in the form of electromagnetic radiation, called Bremsstrahlung. A fast electron displaces an inner shell electron (blue), leaving a vacancy. This vacancy is filled by a higher shell electron, which produces electromagnetic radiation based on the energy difference between the two shells, called characteristic.

Bremsstrahlung is not quantized because there are infinite ways that an electron can be deflected by the anode material. This also means that this type of radiation is a broad spectrum of different energies that span over a wide range, as pictured in Figure 3.

In the case of characteristic x-rays, a different mechanism controls the type of radiation produced. When the fast electrons come into contact with the atoms of the anode material, some of them will not be deflected. Rather, some electrons could knock out inner shell electrons from the atoms as shown in Figure 11. Once there is a hole or vacancy in a lower shell, a higher shell electron can fill in the vacancy. According to Max Plank and Albert Einstein from Equation (33), differing wavelengths correspond to differing energies. The electron loses energy when falling to a lower shell, and the difference in energy is released as an electromagnetic wave. Because of the specific energies produced in this way, characteristic radiation is sharply defined as seen in Figure 3. Then, it is possible to distinguish characteristic radiation from Bremsstrahlung when analyzing an intensity spectrum from a diffractometer.

Chapter 3

XRD APPARATUS

3.1. Houghton XRD

X-rays are produced in an x-ray tube and reflect off of a sample at the center of a semicircular table, pictured in Figure 12. A detector counts reflected rays. The sample and detector are mounted to two arms which rotate the table about an axis through the sample. Motors control the movement of the arms, and rotary encoders keep track of their angular position. The entire apparatus is encased in a 3 mm thick steel box, with the additional safety precaution of lead bricks 5 cm thick blocking the x-ray beam from exiting the box.

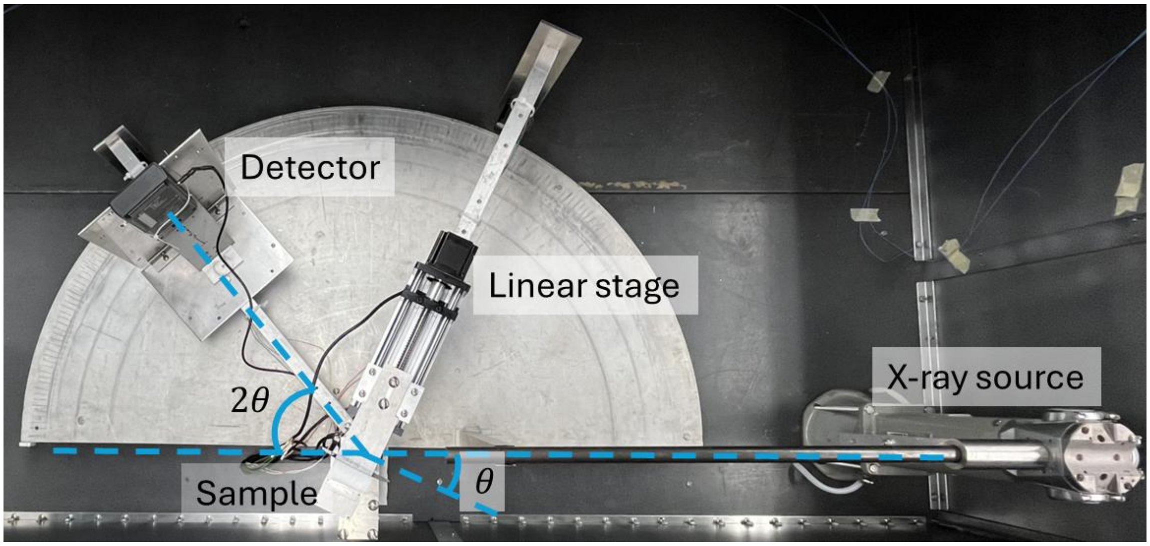

Figure 12. Houghton XRD. Top view the x-ray tube (right) with a steel collimating tube that extends to the sample. The linear sample stage is mounted to the sample arm and moves the sample in and out of the x-ray path. The detector is mounted to the detector arm.

3.1.1. Components

X-rays are produced with a Norelco Diffraction Tube [20] as seen in Figure 13. The photograph and diagram both show the tube upside-down. X-rays are produced when electrons from filament K accelerate and hit anode A, which is made of Cu. On the tube, windows V1 and V3 give a square collimation slit (1.6 mm x 1.6 mm) while windows V2 and

V4 give a horizontal thin collimating slit (10 mm x 0.16 mm). The x-ray source that is pictured in Figure 12 holds the tube and provides covers to block all but one window, restricting x-rays to one direction. In this case, x-rays exit window V1. To collimate the x-rays further than the windows, a 63.5 cm long steel pipe is mounted to the x-ray tube window and pointed towards the sample.

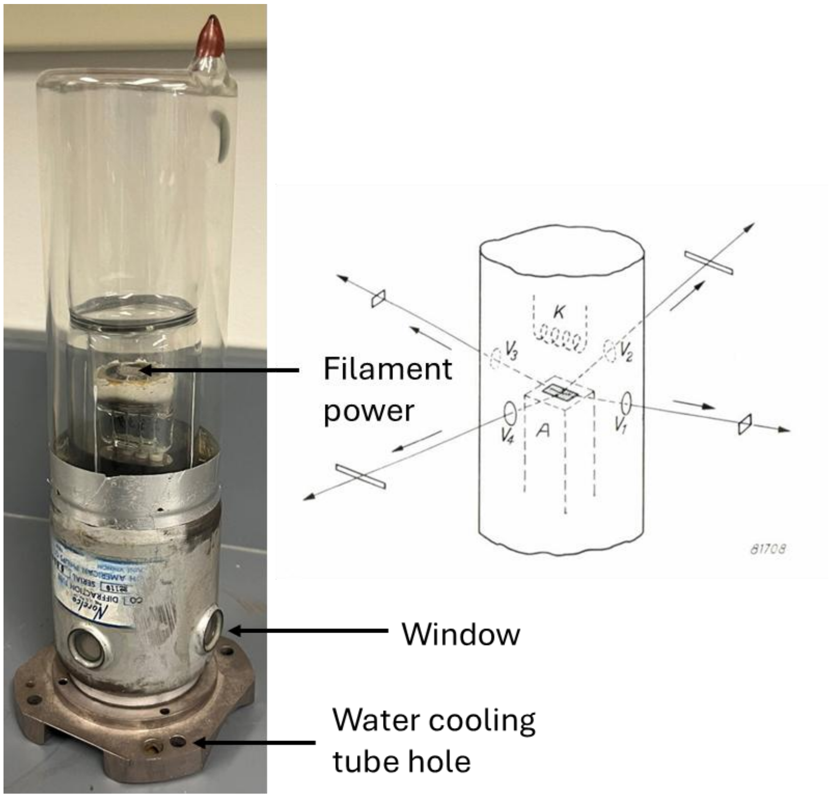

Figure 13. Norelco Diffraction Tube. Picture (left) shows two windows. The filament power is received through the indicated electrode surrounded by glass. Holes for the water-cooling system are shown in the base of the tube. The diagram (right) shows the filament K and target A made of Cu, with the Be windows V1, V2, V3, and V4. Diagram taken from Ref. [20].

Plastic tubing runs from a faucet to the water-cooling system in the tube holder through the bottom of the table and connects to the inlet and outlet copper pipes, pictured in Figure 14. The pipes cycle water up through the base of the x-ray tube and back into a sink to prevent the target from melting.

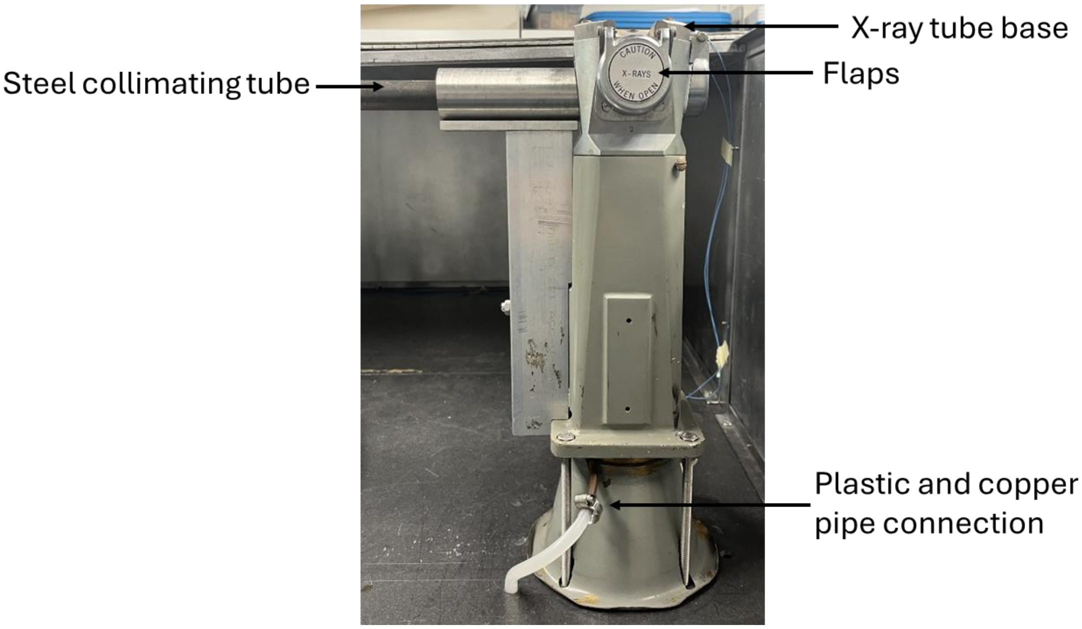

Figure 14. X-ray tube holder. The Tube sits upside down from view in Figure 13 so that x-rays exit windows along line indicated. Flaps cover the other three windows not in use. Plastic tubing feeds from a hole in the table to the water-cooling system. Copper pipes run water up and over the base of the tube to decrease the risk of overheating.

Underneath the table, the power cord feeds through to the tube, a multimeter reads the current from the Drok DC buck converter, all inside a Plexiglas box, seen in Figure 15. A 12 V battery powers a buck converter circuit which provides the filament with current, typically 3 A. The filament is floated at -40 kV with respect to the anode. This strong potential difference is what causes electrons from the filament to accelerate towards the anode and produce x-rays. The high voltage circuit is safely contained inside a Plexiglas box with switches on the door. If opened, the circuit is disconnected and high voltage is shut off. The components inside the box are pushed back away from the door so that no electrons arc to the grounded bolts in the door.

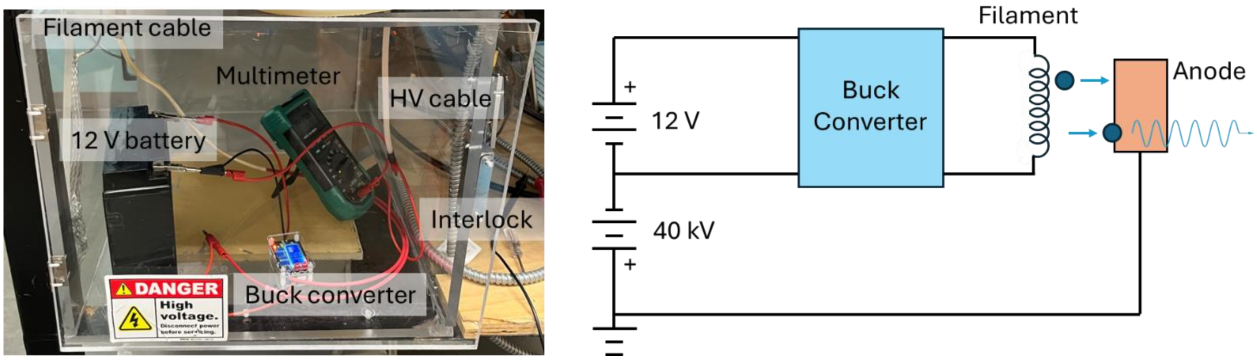

Figure 15. X-ray buck converter circuit.12 V supplied by a battery powers a Drok DC buck converter inside a Plexiglass box, producing 3 A through the filament. The anode inside the x-ray tube is at a 40 kV potential so that electrons from the filament accelerate across the gap and hit the anode to produce x-rays.

The movement of the two arms is controlled by two Lin engineering 101411 stepper motors. The sample and detector arms are held securely to the table via a 35.56 cm long aluminum axle of diameter 1.24 cm pressed into a hole of the same diameter in the center of the semicircle. The top of the axle is held with an aluminum plate as seen in Figure 16 to make sure the axis is stabilized throughout arm movement.

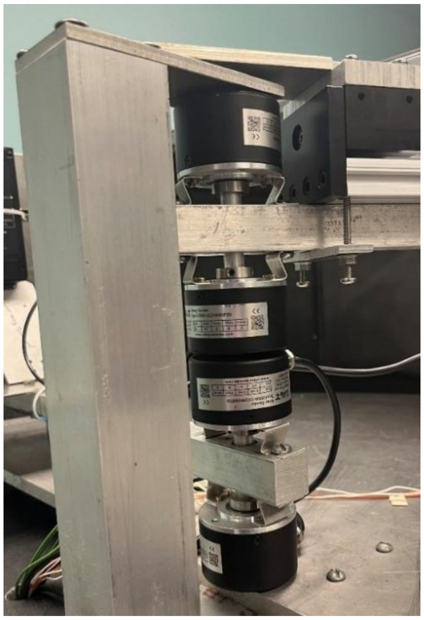

Figure 16. Encoders attached to axle. Four CALT GHH60 rotary encoders are attached to the axel and to the detector and sample arms. A 5.08 x 5.08 x 29.46 cm Al block is holding a 5.08 x 12.7 x 0.64 cm Al plate which secures the axle from moving.

The rotating center pieces of four CALT GHH60 rotary encoders are attached to the 1.24 cm diameter axle with set screws. The top two encoders are also attached to the sample arm with aluminum mounts. The bottom two are likewise attached to the detector arm. There are two encoders for each arm to make an average evaluation of the angular positions. Each has 2000 encoder triggers per 90° of rotation. Two encoders for each arm increases the resolution to 4000 triggers per 90°.

The detector is a Vernier Student Radiation Monitor Geiger tube that is able to detect beta particles, gamma-rays, and x-rays, seen in Figure 17. The detector converts ionizing radiation interactions to electric pulses, which are sent through an audio cable. It is secured to the arm with a clamp.

Figure 17. Geiger Tube Detector. A battery powered Geiger tube capable of detecting beta, gamma, and x-ray radiation can send the number counts via electric pulses.

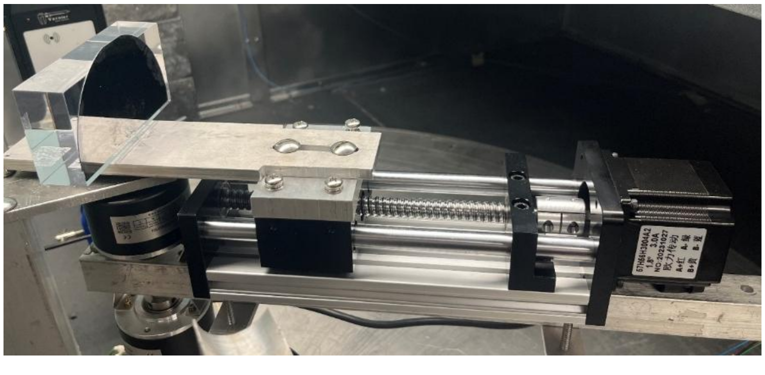

Figure 18. Linear sample stage. A NEMA 23 stepper motor capable of moving 100 mm with 1600 steps/mm. The sample is held on an acrylic block.

A ball screw linear translation stage that centers the sample in the x-ray beam is seen in Figure 18. A NEMA 23 stepper motor rotates the threaded axil to move the ball screw. The rotating motor winds and screw so that the stage can move back and forth through the path of x-rays. Once the power is on and x-rays are being produced, the steel box can close around the apparatus. The sample will be centered in the beam with the detector at 0°. An acrylic block is used as a backing to the thin film sample which sits on the stage seen in Figure 18. The block stops about 50 % of x-rays to the detector. This allows for the sample to be aligned to the middle of the x-ray beam, as it is about half an inch in width.

The encoders and motors are controlled by a Teensy 4.1 microcontroller which sits under the table in a circuit box as seen in Figure 19. The wires feed through a hole in the table.

The Teensy is powered by 5 V but accepts and returns voltages of 3.3 V, shown by the flow chart in Figure 19. The motor controllers need 5 V to run, and the encoders produce 5 V digital pulses. Therefore, voltage converters and a buffer are needed. The voltage converters (HiLetGo Logic Level Bi-Directional Converters) change a 5 V input to a 3.3 V output. There are three converters needed for the encoder output wires. The buffer is a SN74ACT241N digital chip which takes 3.3 V and converts to the 5 V operating voltage to power the motor controllers.

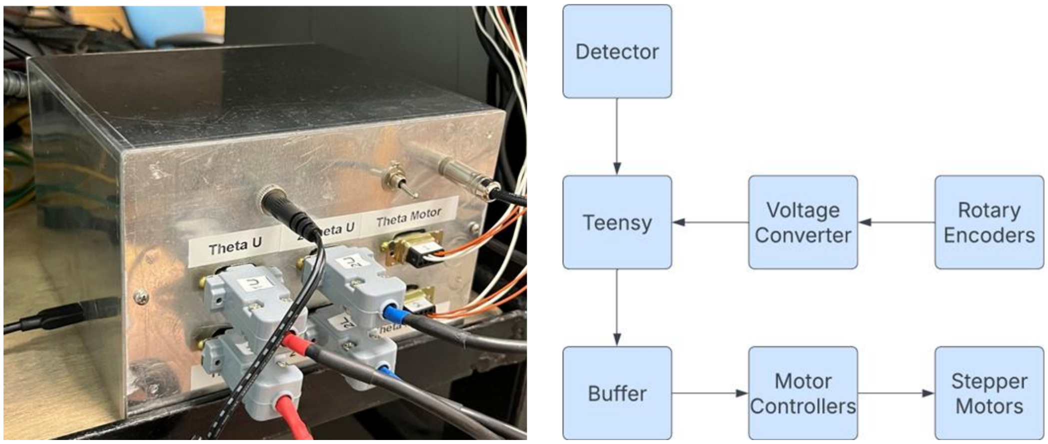

Figure 19. Circuit box and circuit flow chart. Picture (left) shows the outside of the circuit box which houses a Teensy, buffer, three voltages converters, and three motor controllers. Four encoder and three motor wires plug into the box, as well as the detector output. The Teensy is powered and controlled through a computer via a micro-USB to USB cable seen on the left side of the box.

3.1.2. Encoder Array

The number of motor steps is used to keep track of the positions of the arms (theta and 2-theta) and the sample stage (z). The theta and 2-theta motors have rubber O-rings around their axles to act as tires when they rotate around the table. However, the tires are prone to slipping, so there is systematic uncertainty that increases with more steps taken. The rotary encoders are used to account and correct this. Each encoder has a set 2000 positions per 90°. For one arm, there are two encoders, so there are 4000 positions per 90°. The average number of steps between each encoder position is about 66, seen from Figure 20, showing that the steps are a measure of the angular distance between encoder positions.

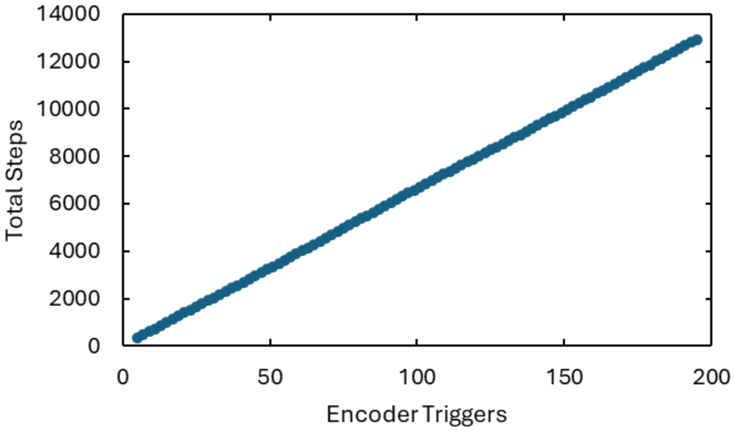

Figure 20. Total steps vs. encoder position plot. Specific data is from theta arm motor and the upper encoder. The general linear nature of the plot gives evidence that the average rate of motor steps is approximately constant at 66.2 microsteps.

Now, the angular positions of the arms can be tracked in motor steps if the angular distance between encoder positions is repeatable. However, these encoder positions are not spaced evenly, which can be verified by counting the number of motor steps taken between each encoder position, seen in Table 1. Ten scans of the theta arm were taken and the average number of motor steps were recorded between each encoder trigger. The steps are closely repeatable as seen from the low standard deviations, which shows that motor slippage is rare. Therefore, the angular positions of the arms can now be measured in motor steps, which are separated by a much smaller angular distance than encoder positions.

To figure out how many steps are between each encoder position, an encoder array was created. The number of motor steps are recorded until a new encoder trigger. By running the program through multiple scans, an average number of steps between each encoder position was established. An array was constructed by scanning the theta and 2-theta arms 155° around the table, which is almost 69000 encoder triggers. The detector arm started at 0° and the sample arm started at -80°. The average of 10 scans of the array is partially shown in Table 1. Between each encoder position for the 10 scans, the average was consistent, giving a standard deviation of about 2 for each position. The average steps through positions fluctuated but repeated every 8 positions. While there is a different number of steps between encoder positions, the low standard deviation for each encoder position shows that it is repeatable.

Table 1. Encoder array. Ten scans from theta arm encoders with the number of steps recorded for each encoder position (each row). The averages of each row and their standard deviations are recorded. The pattern of values repeats every eight encoder positions, indicated to the right.

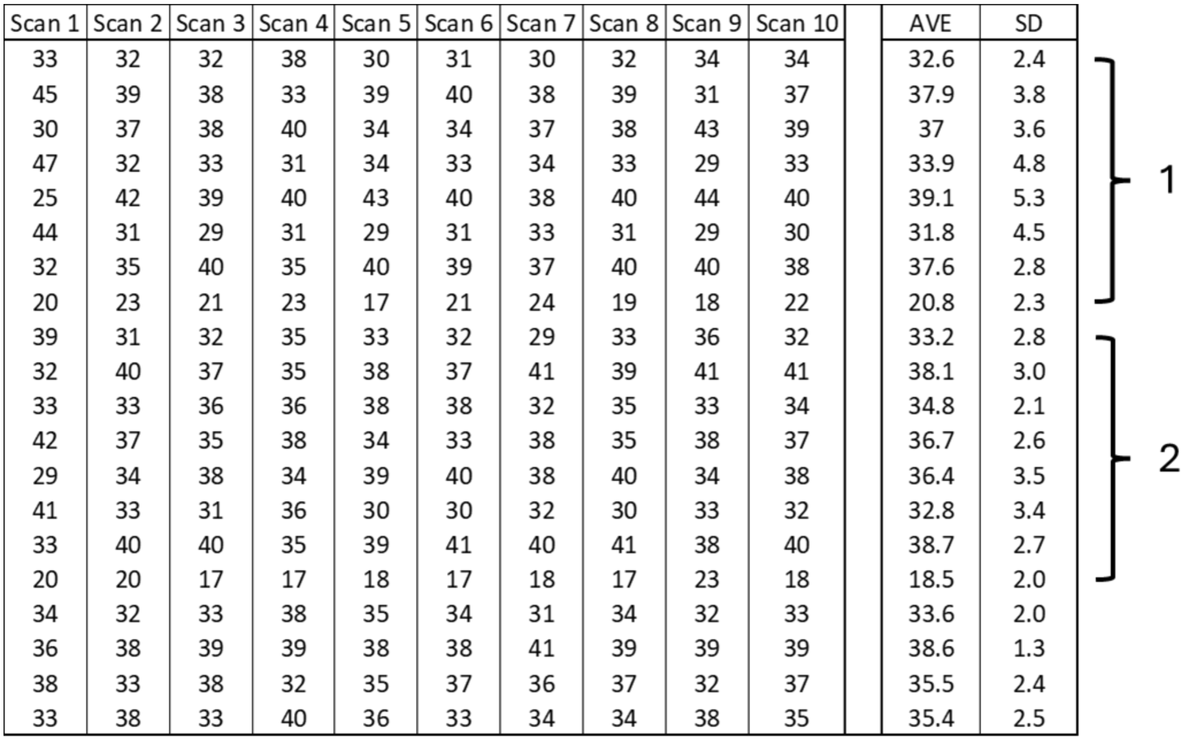

Scan 1	Scan 2	Scan 3	Scan 4	Scan 5	Scan 6	Scan 7	Scan 8	Scan 9	Scan 10		AVE	SD
33	32	32	38	30	31	30	32	34	34		32.6	2.4
45	39	38	33	39	40	38	39	31	37		37.9	3.8
30	37	38	40	34	34	37	38	43	39		37	3.6
47	32	33	31	34	33	34	33	29	33		33.9	4.8
25	42	39	40	43	40	38	40	44	40		39.1	5.3
44	31	29	31	29	31	33	31	29	30		31.8	4.5
32	35	40	35	40	39	37	40	40	38		37.6	2.8
20	23	21	23	17	21	24	19	18	22		20.8	2.3
39	31	32	35	33	32	29	33	36	32		33.2	2.8
32	40	37	35	38	37	41	39	41	41		38.1	3.0
33	33	36	36	38	38	32	35	33	34		34.8	2.1
42	37	35	38	34	33	38	35	38	37		36.7	2.6
29	34	38	34	39	40	38	40	34	38		36.4	3.5
41	33	31	36	30	30	32	30	33	32		32.8	3.4
33	40	40	35	39	41	40	41	38	40		38.7	2.7
20	20	17	17	18	17	18	17	23	18		18.5	2.0
34	32	33	38	35	34	31	34	32	33		33.6	2.0
36	38	39	39	38	38	41	39	39	39		38.6	1.3
38	33	38	32	35	37	36	37	32	37		35.5	2.4
33	38	33	40	36	33	34	34	38	35		35.4	2.5

Now the positions of the arms are well estimated. The theta and two theta encoder arrays (sample arm and detector arm) are now also recorded, with similar results. The average number of steps per encoder position is 33 for each encoder. Now, even though there are a different number of steps between each encoder position, the angular position of each arm can be known. The encoder array is implemented in an Arduino code that runs on the Teensy. When the arms are instructed to move to a certain angle, the motors move until the position is confirmed by the encoders. This way, even if the motors slip and rotate more than they should, the encoders know the approximate spot in the array it is at. The uncertainty in the angular position of the sample arm is the standard deviation for each encoder trigger. It is the same for the detector arm, but a separate encoder array for the sample encoders and motor. The average uncertainty for the theta arm position is ±1.7 steps, and ±2.3 for the 2-theta arm. This means that for each encoder trigger, there is about 1.1 to 1.6 m° of uncertainty for the theta and 2-theta arm, respectively.

Even though the encoder array is used to determine the angular position of the arms, the starting position of the arms is unknown unless they are physically moved there. However, the encoders have a Z trigger at one position that is used for aligning the arms before a scan. The arms will move until Z theta is found, then Z 2-theta. This can be used to align the arms. The Z position for theta is -23° and Z 2-theta is 81°. Once the arms are aligned, they can move to anywhere on the table to start a scan.

Chapter 4

XRD SCANS

4.1. Pre-Scan and Alignment Procedure

The Houghton XRD was used to find the orientations for thin Ag films of unknown thickness made in the Houghton University deposition chamber. The Ag was deposited on a Si glass substrate. The sample was attached to the acetal block on the sample stage using double-sided tape. The detector and sample arms were placed at 0°, meaning that the detector was in line with the incident x-ray beam and the sample was parallel to the beam. The filament current was slowly increased to 3 A and with high voltage on, the emission current was 8 mA.

The detector arm was aligned so that it starts a scan from the middle of the incident x-ray beam. To do this, the sample stage (z) moves so the sample is completely out of the way of the beam. Then, the detector arm was scanned from -1° to 5°. This resulted in the plot shown in Figure 21.

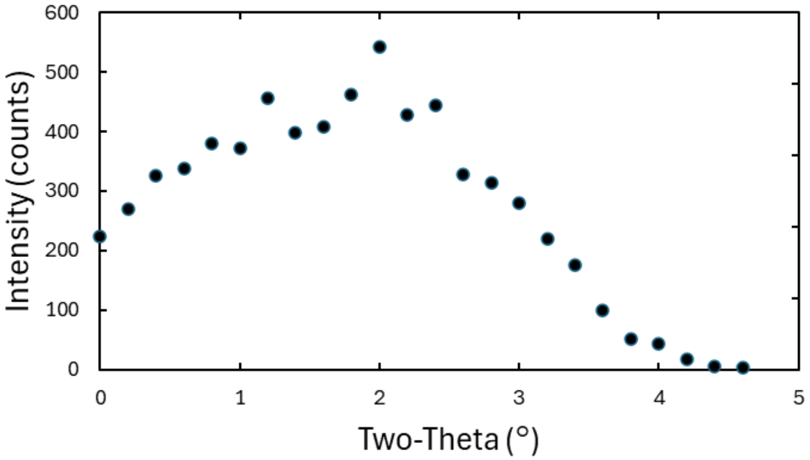

Figure 21. Detector alignment. A scan of the detector arm from 0° to 5° shows that the intensity of x-rays increased then decreased as the detector moved in and out of the beam. The detector arm angle was zeroed at the point of maximum intensity.

The intensity of x-rays increased to about 530 counts at about 2° then decreased. When the detector area moved from the left of the beam to the right of the beam, the intensity of x-rays displayed a bell curve form. The maximum point of the curve is where the beam was hitting the detector fully. This is where the detector angle was zeroed. The detector was moved to the new zero position for future alignment and scans.

For aligning z, the motor scanned from 0 mm to 50 mm, or where the sample was to the left of the beam, to where the sample was to the right of the beam. A plot of intensity vs. distance is in Figure 22.

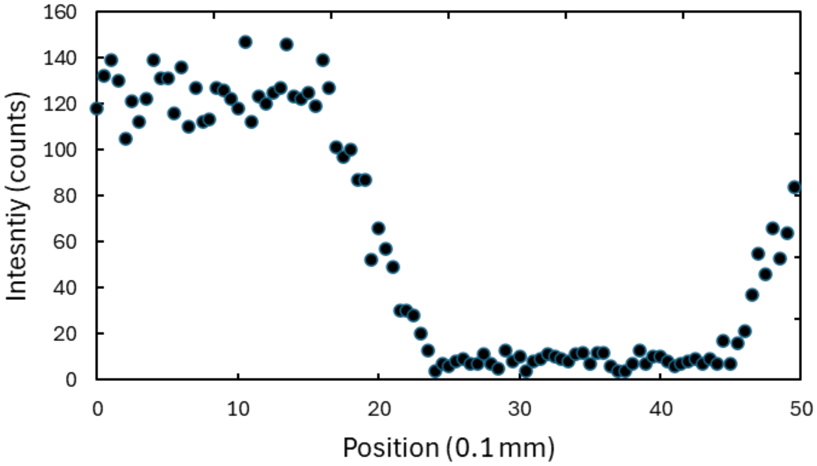

Figure 22. Z alignment. The linear sample stage was moved from 0 mm to 50 mm. The intensity was highest from 0 to 15 mm where nothing was blocking the beam path to the detector. The intensity fell off approximately linearly because the x-rays were being absorbed by the acetal block which held the sample. At around 45°, the intensity increased again because the acrylic was no longer blocking the detector.

The intensity of x-rays was highest when the sample was not blocking the path of x-rays to the detector. Once the sample and acrylic block intersected the beam, the intensity began to decrease reasonably linearly because the x-rays were being partially absorbed by the acetal. The intensity began to decrease at about 16 mm and stopped decreasing at about 24 mm. This means that the sample was in the approximate middle of the beam at the halfway point of the line. So, z was zeroed at 20 mm.

Next, the sample arm was aligned. The position of this arm controls the angle of the sample relative to the x-ray beam. To align this arm, the sample arm was scanned from -5° to 5°. The intensity of x-rays looked like a bell curve because the beam follows a probability distribution. Then, the sample arm was zeroed to the point where the intensity was a maximum, as seen in Figure 23.

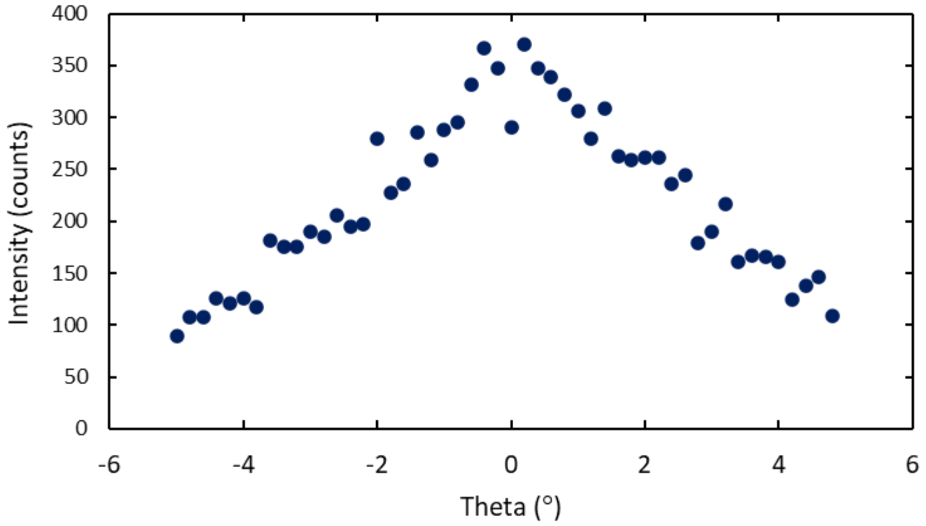

Figure 23. Theta alignment. The sample arm was scanned from -5° to 5°. The intensity of x-rays increased and decreased about zero because the sample let the most amount of x-rays pass when parallel to the beam.

The process of aligning z and the sample arm went back and forth until they were both aligned at the same time. This was necessary because once the sample stage was aligned, the theta alignment could have changed, and vice versa. All the motors should be at their zeroed positions then. Finally, the XRD can make a scan of a thin film to find the crystal orientations. Unfortunately, the x-ray tubes were not producing a significant amount of radiation for significant data.

Chapter 5

CURRENT STATUS AND FUTURE PLANS

There have been many improvements made to Houghton University's XRD in this research timeframe. Four new rotary encoders were implemented on the machine to more accurately determine the angular positions of the detector and sample arms. A new circuit and Teensy 4.1 microcontroller were implemented to control the movement of the arms and data collection. The motors have been shown to have small slippages that add a systematic uncertainty to their angular positions. An encoder array was made to account for this, which relies on the consistent encoder positions. Alignment of the arms for the pre-scan procedure was shown possible.

Currently, the intensity of x-rays produced by a Cu and Mo tube is several orders of magnitude below expected. There are many reasons why this could happen, such as air in the x-ray tube, broken filament, or poor alignment. Until a solution is found, no significant data can be collected.

Once that issue is solved, the future plans for the Houghton XRD will start with mounting a second linear stage to the first linear stage. Then, the x-direction and z-direction of the sample with respect to the beam can be controlled. Then, different samples can be studied easily by moving the stage in the x-direction so the beam hits a different sample mounted to it. Next, a new detector that has an energy resolution would help separate any background radiation from the desired data. Additionally, a new detector with a smaller width would improve angular precision. Finally, replacing the 12 V battery with a voltage transformer would allow for longer scans as there is no time when the transformer needs to be recharged like the battery does.

References

---

[1] W. Crookes, On Radiant Matter, (Lecture given at the British Association for the Advancement of Science, 1912).
[2] W.C. Rontgen, *Ueber eine neue Art von Strahlen*, *Sitzungsherichten der Wurzburger Physik-medic*, **1895**, 1 (1895).
[3] W. C. Rontgen, *On a New Kind of Rays*, *Science*, **3**, 227 (1896).
[4] B. H. Broadbent, *A New X-Ray Technique and its Application to Orthodontia*, *The Angle Orthodontist*, **1**, 45 (1931).
[5] J. C. Maxwell, *A Dynamical Theory of Electromagnetic Waves*, *Phil. Trans*., **155**, 459 (1865).
[6] A. Sommerfeld, H. L. Brose Trans., "Atomic Structure and Spectral Lines", (E. P. Dutton and Company, New York, NY, 1919).
[7] W. Friedrich, P. Knipping, M. Laue, *Interference Phenomena for X-rays*, in *Structural Crystallography in Chemistry and Biology*, trans. J. J. Stezowski (Hutchinson Ross Publishing Company, Stroudsburg, PA, 1912), p. 23-39.
[8] M. A. Bravais, *On the Systems Formed by Points Regularly Distributed on a Plane or in Space*, Trans. A. J. Shaler (Dover Publication, Mineola, NY, 2005).
[9] W. Friedrich, P. Knipping, M. Laue, *Interferenzerscheinungen bei Rontgenstrahlen*, *Annalen der Physik*, **346**, 971 (1912).
[10] W. H. Miller, "Treatise on Crystallography", (J. & J. J. Deighton, John W. Parker, Cambridge and London, 1839).
[11] W. H. Bragg, W. L. Bragg, "X-rays and Crystal Structure", (G. Bell and Sons, London, 1915).
[12] W. Wood, *Differences in the Structure of Electrodeposited Metallic Coatings shown by X-ray Diffraction*, *Transactions of the Faraday Society*, **31**, 1248 (1935).
[13] P. Sherrer, *Bestimmung der Grösse und der inneren Struktur von Kolloidteilchen mittels Röntgenstrahlen*, Nachrichten von der Gesellschaft der Wissenschaften zu Göttingen, Mathematisch-Physikalische Klasse, **1918**, 98 (1918)
[14] T. Ohmi et al, *Formation of Copper Thin Films by a Low Kinetic Energy Particle Process*, Abstract, *J. Electrochem. Soc*., **138**, 1089 (1991).
[15] J. L. Heerden, R. Swanepoel, *XRD Analysis of ZnO Thin Films Prepared by Spay Pyrolysis*, *Thin Solid Films*, **299**, 72 (1997).
[16] J. Greiser, D. Müller, P. Müller, C. V. Thompson, E. Arzt, *Growth of Giant Grains in Silver Thin Films*, Abstract, Scripta Materialia, **41**, 709 (1999).
[17] P. Sonnweber-Ribic, P. A. Gruber, G. Dehm, H. P. Strunk, E. Arzt, *Kinetics and Driving Forces of Abnormal Grain Growth in Thin Cu Films*, Abstract, *Acta Materialia*, **60**, 2397 (2012).
[18] S. P. Baker, B. Hoffman, L. Timian, A. Silvernail, E. A. Ellis, *Texture Transformations in Ag Thin Films*, *Acta Materialia*, **61**, 7121 (2013).
[19] E. A. Ellis et al, *Driving Forces for Texture Transformation in Thin Ag Films*, *Acta Materialia*, **105**, 495 (2016).
[20] W. Parrish, E. Hamacher, K. Lowitzsch, *The 'Norelco' X-ray Diffractometer*, *Philips Tech. Rev*., **16**, 123 (1954).